Spin-dependent scattering and the spin polarization of a diffusive current in partly disordered L1 0 epitaxial FePd

K Seemann, C H Hickey, Vincent Baltz, B J Hickey, C H Marrows

Spin-dependent scattering and the spin polarization of a diffusive current in partly disordered $L1_0$ epitaxial FePd

2010 New J. Phys. 12 033033

(http://iopscience.iop.org/1367-2630/12/3/033033)

New Journal of Physics
The open-access journal for physics

Spin-dependent scattering and the spin polarization of a diffusive current in partly disordered $L1_0$ epitaxial FePd

K M Seemann[1,2], M C Hickey[3], V Baltz[4], B J Hickey and C H Marrows[2]

School of Physics and Astronomy, University of Leeds, Leeds LS2 9JT, UK
E-mail: k.seemann@fz-juelich.de and c.h.marrows@leeds.ac.uk

New Journal of Physics **12** (2010) 033033 (19pp)
Received 16 October 2009
Published 16 March 2010
Online at http://www.njp.org/
doi:10.1088/1367-2630/12/3/033033

Abstract. We report magnetic domain wall (DW) resistance in epitaxial films of FePd. When equal numbers of Fe and Pd atoms are present, this material forms an ordered structure with alternating crystal planes of Fe and Pd. We prepared films enriched with Pd to varying degrees, gradually degrading this structure. As might be expected, this increased the electrical resistivity of the films by introducing extra defects that can scatter electrons. However, unexpectedly, the additional resistance arising from the ∼10 nm thick DWs rose as a proportion of the overall resistivity, roughly doubling when halving the degree of chemical ordering—as determined from x-ray diffraction measurements—within the films. These data can be used to infer a rise in the spin polarization of the current flowing in the layers when extra Pd atoms are introduced. On the other hand, a separate measurement of spin polarization using a superconducting point contact technique that is insensitive to electron scattering revealed no changes as extra Pd was introduced. We conclude that Pd atoms scatter electrons of one spin far more strongly than the other, suggesting a possible means of producing highly spin-polarized currents for use in spintronic devices.

S Online supplementary data available from stacks.iop.org/NJP/12/033033/mmedia

[1] Present address: Institut für Festkörperforschung (IFF-9), FZ Jülich GmbH, D-52425 Jülich, Germany.
[2] Authors to whom any correspondence should be addressed.
[3] Present address: Department of Physics, University of Massachusetts Lowell, One University Avenue, Lowell, MA 01854, USA.
[4] Present address: INAC/SPINTEC (URA CEA/CNRS 2512), CEA Grenoble, 17 Avenue Martyrs, 38054 Grenoble Cedex 9, France.

Contents

1. Introduction

Using the spin degree of freedom of the electron to store and process information, just as charge is used in the current generation of microelectronic devices, is the central concept of spintronics [1]. The proposal of the spin field-effect transistor by Datta and Das [2], which relies on generating, manipulating and detecting spin-polarized currents, triggered enormous activity and effort to understand and control spin-dependent transport. An area of active interest at present is domain wall (DW) spintronics [3], where spin-polarized currents interact with local gradients in the magnetization direction, giving rise to additional resistance [4, 5] and spin-transfer torques [6, 7].

The Stoner model of itinerant ferromagnetism describes magnetization as arising from two separate populations of electrons, spin-↑ and spin-↓, the first of which is greater in total number [8]. These may conduct in parallel [9], and the resulting difference in conductivity due to the different sub-band structures at the Fermi level will lead to an imbalance in the proportion of current carried by the two spin species. A key parameter in quantifying this is the degree of spin polarization P of the current that flows, and hence a proper definition of P in the appropriate transport regime is required [10, 11]. P is defined as the unpaired fraction of the current when resolved into contributions to the current density J carried by the spin-↑ and spin-↓ carrier populations, $P = (J_\uparrow - J_\downarrow)/(J_\uparrow + J_\downarrow)$. Since these current densities are driven by the same electric field $\mathcal{E}$, we can use Ohm's law $J = \sigma\mathcal{E}$ to write the formula in terms of spin-resolved conductivities, $P = (\sigma_\uparrow - \sigma_\downarrow)/(\sigma_\uparrow + \sigma_\downarrow)$. Determining P now amounts to finding an expression, appropriate for the transport regime in question, for these conductivities. In a ballistic experiment, such as PCAR spectroscopy [12, 13], these will be determined solely by the spin-dependent electronic structure. In the diffusive regime the spin-dependent scattering rates $1/\tau_{\uparrow(\downarrow)}$ will also play a role. Equivalently, one can define a spin asymmetry $\alpha = \sigma_\uparrow/\sigma_\downarrow$, straightforwardly related to the polarization by

$$P = \frac{\alpha - 1}{\alpha + 1}. \tag{1}$$

For instance, in the common method of measuring spin polarization, PCAR [12, 13], the polarization of a ballistic current crossing an interface from the ferromagnet in question into a superconductor is measured. In the ballistic limit, following the ideas of Mazin [10], we define

$$\alpha_{\text{ballistic}} = \frac{g_\uparrow(E_\text{F})v_{\text{F},\uparrow}}{g_\downarrow(E_\text{F})v_{\text{F},\downarrow}}, \tag{2}$$

which depends only on the spin-resolved densities of states at the Fermi level $g_{\uparrow,\downarrow}(E_F)$ and Fermi velocities $v_{F,\uparrow,\downarrow}$.

Meanwhile, in the diffusive regime the spin-dependent relaxation times $\tau_{\uparrow,\downarrow}$ must also be taken into account. Using a simple Drude expression for the conductivity, we may write

$$\alpha_{\text{diffusive}} = \frac{g_{\uparrow}(E_F)v_{F,\uparrow}^2\tau_{\uparrow}}{g_{\downarrow}(E_F)v_{F,\downarrow}^2\tau_{\downarrow}}. \tag{3}$$

These spin-dependent scattering rates mean that a transport current may have a different degree of spin polarization to the underlying carrier densities, as the two species will have different mobilities. The expressions for current polarization in the ballistic ($P_{\text{ballistic}}$) and diffusive ($P_{\text{diffusive}}$) regimes follow easily from equation (1).

Here, we report on the role of spin-dependent impurity scattering in the spin polarization of a diffusive current $P_{\text{diffusive}}$ in ferromagnetic $L1_0$-ordered $Fe_{(1-x)}Pd_x$ epilayers, whose crystal structure gives rise to a strong magnetic easy axis that is oriented perpendicular to the film plane, yielding dense, narrow DWs. The chemical order parameter S was reduced by varying x. We measured the DW magnetoresistance (MR) to quantify $P_{\text{diffusive}}$ using the Levy–Zhang (LZ) theory of DW MR [5, 14], while we used PCAR conductance spectroscopy to address the ballistic case. We show that the extra Pd atoms act as spin-dependent scattering centres, changing the scattering rates $1/\tau_{\uparrow,\downarrow}$, in such a way as to give both higher resistivity and DW MR. As might be expected, the PCAR results are unaffected by the changes in $\tau_{\uparrow,\downarrow}$.

2. Sample preparation and structural and magnetic characterization

Samples were prepared by conventional dc magnetron sputter co-deposition on polished MgO(001) substrates, i.e. Fe and Pd were deposited simultaneously from separate targets. Varying the power applied to the two targets changed the Pd content x. Thin films were sputtered directly onto the substrates at a substrate temperature of ~1000 K and at a deposition rate of 0.1–0.2 Å s^{-1} without relying on the seeding underlayer. We used a 4%-hydrogen-in-argon sputter gas mixture to prevent any film oxidation during growth at high temperatures. High-resolution transmission electron microscopy has previously been used to demonstrate the high degree of epitaxy achieved by this growth process [11]. Low-angle x-ray reflectometry measurements showed that film thicknesses were in the range $t = 30 \pm 3$ nm for all four samples. We describe their structural and magnetic properties in the following.

Central to this work is a precise understanding of the crystallographic long-range ordering in $Fe_{1-x}Pd_x$ films on enrichment with Pd. Consequently, we determined for each of our four samples studied here a crystallographic long-range order parameter S, which is defined as $S = r_\alpha + r_\beta - 1 = (r_\alpha - x_A)/y_\beta = (r_\beta - x_B)/y_\alpha$, with $0 \leqslant S \leqslant 1$. Here x_A and x_B are atomic fractions of the two species, y_α and y_β are fractions of the lattice site types α and β in the ordered structure, and r_α and r_β are fractions of each type of lattice site occupied by the correct types of atoms, A on α and B on β [15–17]. For a perfectly ordered film, $r_\alpha = 1$, $r_\beta = 1$, which consequently yields $S = 1$, while a random distribution of atoms over lattice sites leads to $S = 0$.

More practically, however, S is determined from the relative intensities and the positions of the (001) peak and the (002) peak obtained from Θ–2Θ x-ray diffraction scans. We carried out Θ–2Θ scans for each sample using Cu-K_α radiation, i.e. $\lambda = 1.541$ Å. The Θ–2Θ x-ray diffraction scan of the FePd film with a nominally equiatomic composition level is exemplified in figure 1(a) together with a scan of the bare MgO(001) substrate in order to identify diffraction

peaks of the epitaxial thin film unambiguously. Both the (001) peak and the (002) peak are pronounced and are regarded as the hallmark for the face-centred tetragonal $L1_0$ phase of FePd. The presence of the (001) peak is normally forbidden for face-centred crystal lattices, and so its observation here confirms that there is preferential ordering on the alternating α and β planes, which breaks the symmetry of the structure factor. To compute the chemical order parameter S ($0 \leqslant S \leqslant 1$), one has to relate the integrated intensities $\int I_{(001)}(\Theta)\,\mathrm{d}\Theta$ and $\int I_{(002)}(\Theta)\,\mathrm{d}\Theta$ as well as positions of the (001) peak and the (002) peak according to [15]

$$
\begin{aligned}
S^2 = {} & \frac{\int I_{(001)}(\Theta)\,\mathrm{d}\Theta}{\int I_{(002)}(\Theta)\,\mathrm{d}\Theta} \times \frac{\frac{1+\cos^2(2\Theta_{(002)})}{2\sin(2\Theta_{(002)})}}{\frac{1+\cos^2(2\Theta_{(001)})}{2\sin(2\Theta_{(001)})}} \\
& \times \frac{\left(4\sum_{i=1}^{4} a_i^{\mathrm{Fe}} \mathrm{e}^{-b_i^{\mathrm{Fe}}\sin^2(\Theta_{(002)})/\lambda^2} + c^{\mathrm{Fe}}\right) \mathrm{e}^{-(B_0^{\mathrm{Fe}}+B_{293}^{\mathrm{Fe}})\sin(\Theta_{(002)})/\lambda^2}}{\left(\sum_{i=1}^{4} a_i^{\mathrm{Fe}} \mathrm{e}^{-b_i^{\mathrm{Fe}}\sin^2(\Theta_{(001)})/\lambda^2} + c^{\mathrm{Fe}}\right) \mathrm{e}^{-(B_0^{\mathrm{Fe}}+B_{293}^{\mathrm{Fe}})\sin(\Theta_{(001)})/\lambda^2}} \\
& \times \frac{\left(\sum_{i=1}^{4} a_i^{\mathrm{Pd}} \mathrm{e}^{-b_i^{\mathrm{Pd}}\sin^2(\Theta_{(002)})/\lambda^2} + c^{\mathrm{Pd}}\right) \mathrm{e}^{-(B_0^{\mathrm{Pd}}+B_{293}^{\mathrm{Pd}})\sin(\Theta_{(002)})/\lambda^2} + \ldots}{\left(\sum_{i=1}^{4} a_i^{\mathrm{Pd}} \mathrm{e}^{-b_i^{\mathrm{Pd}}\sin^2(\Theta_{(001)})/\lambda^2} + c^{\mathrm{Pd}}\right) \mathrm{e}^{-(B_0^{\mathrm{Pd}}+B_{293}^{\mathrm{Pd}})\sin(\Theta_{(001)})/\lambda^2} + \ldots} \\
& \frac{\ldots + \Delta_{(002)}^{\mathrm{Fe}} \mathrm{e}^{(-B_0^{\mathrm{Fe}}+B_{293}^{\mathrm{Fe}})\sin^2(\Theta_{(002)})/\lambda^2)^2} + \Delta_{(002)}^{\mathrm{Pd}} \mathrm{e}^{(-B_0^{\mathrm{Pd}}+B_{293}^{\mathrm{Pd}})\sin^2(\Theta_{(002)})/\lambda^2)^2}}{\ldots + \Delta_{(001)}^{\mathrm{Fe}} \mathrm{e}^{(-B_0^{\mathrm{Fe}}+B_{293}^{\mathrm{Fe}})\sin^2(\Theta_{(001)})/\lambda^2)^2} + \Delta_{(001)}^{\mathrm{Pd}} \mathrm{e}^{(-B_0^{\mathrm{Pd}}+B_{293}^{\mathrm{Pd}})\sin^2(\Theta_{(001)})/\lambda^2)^2}},
\end{aligned}
\tag{4}
$$

where a_i, b_i and c are coefficients for the analytical approximation of the scattering factors for Pd and Fe (with Δ the imaginary part) [16], and B_0 and B_{293} are the Debye parameters for Pd and Fe [17]. Figure 1(b) illustrates the (001) superlattice x-ray diffraction peaks of each sample normalized to a common (002) peak, i.e. the (002) peaks of all four samples have been scaled to one and the same height. Then the maximal (001) peak height serves as one indicator for the chemical ordering of the film. Employing equation (4) yields the value S for each sample, more precisely $S \in \{0.39, 0.53, 0.72, 0.80\}$, the latter value for a nominally equiatomic film, and the degree of ordering declines as the films are enriched with Pd. This enables us to attribute our magnetic and electron transport parameters, which we will discuss further below, directly to the degree of $L1_0$ ordering in each sample.

In order to estimate the Pd content x, we have performed an x-ray photoelectron spectroscopy (XPS) analysis of our $L1_0$ $Fe_{(1-x)}Pd_x$ films, comparing the relative intensities of the Fe $2p_{3/2}$ and Pd $3d_{5/2}$ peaks (see supplementary data available at stacks.iop.org/NJP/12/033033/mmedia for examples of raw spectra). In the absence of an FePd standard sample, the absolute uncertainty in x measured by this technique is much larger than the relative uncertainty. Therefore, we assumed that the $S = 0.8$ sample is equiatomic ($x = 0.5$), since this is the highest value of S that we obtained when varying the balance of powers applied to our magnetrons during the trial growths for this study. Other values of x are then given in table 1 relative to this, with relative uncertainty as an error bar. Since these values are not absolute, we retain the experimentally measured quantity S as the most convenient parameter to label our samples.

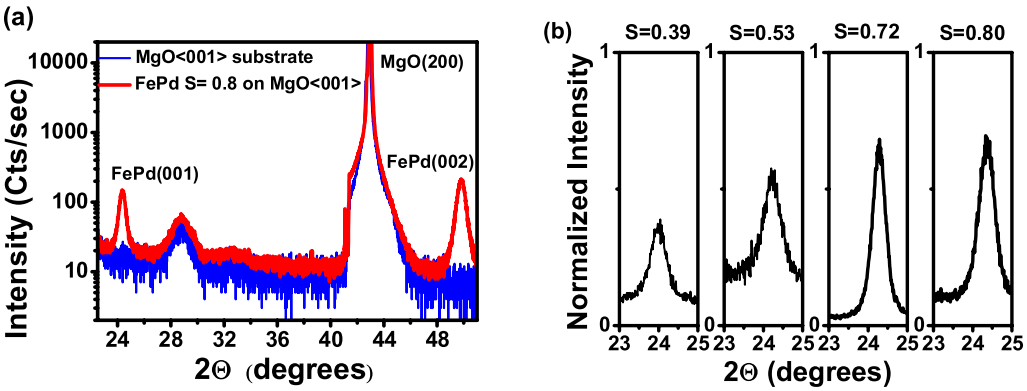

Figure 1. (a) Θ–2Θ x-ray crystallography scan for an $L1_0$-ordered FePd film (red) showing pronounced (001)- and (002)-order Bragg peaks yielding a chemical long-range order parameter of $S = 0.8$. The MgO(001) substrate scan is included for comparison (blue) and allows the identification of all other features in this x-ray scan such as the (200) MgO substrate peak. (b) (001) superlattice x-ray diffraction peaks of each sample normalized to the relevant (002) peak, the peak intensity of which is set to 1. The maximal peak height is one indicator for the chemical ordering of the film; the exact chemical order parameter S, determined from integrated peak intensities as described in the text, is denoted in each case ranging from $S = 0.39$ to 0.8.

Table 1. Structural and magnetic properties of the four $Fe_{1-x}Pd_x$ epilayers studied. The crystallographic long-range ordering S was determined by x-ray diffraction as described in the text, while the relative Pd content x was estimated from XPS spectra. The micromagnetic parameters A, $K_\perp$ and M_s (at 4.5 K) were determined from VSM measurements. The average domain width was determined from MFM experiments $\bar{D}_{MFM}$ and OOMMF simulations $\bar{D}_{sim}$, and an estimated DW width $\delta_W = \pi\sqrt{A/K_\perp}$ is also shown.

S	x	A (pJ m^{-1})	$K_\perp$ (MJ m^{-3})	M_s (MA m^{-1})	$\bar{D}_{MFM}$ (nm)	$\bar{D}_{sim}$ (nm)	δ_W (nm)
0.39 ± 0.05	0.68 ± 0.01	8.1 ± 0.4	0.8 ± 0.1	1.1 ± 0.1	95 ± 10	88 ± 10	10.0 ± 0.9
0.53 ± 0.05	0.64 ± 0.01	10.0 ± 0.1	0.9 ± 0.1	1.2 ± 0.1	93 ± 10	85 ± 10	10.4 ± 0.8
0.72 ± 0.05	0.51 ± 0.01	13.2 ± 0.1	1.2 ± 0.1	1.4 ± 0.1	96 ± 10	83 ± 10	10.4 ± 0.6
0.80 ± 0.05	0.5	16.0 ± 0.6	1.5 ± 0.1	1.5 ± 0.1	91 ± 10	89 ± 10	10.2 ± 0.5

Next, we turn to the magnetic properties of our $Fe_{(1-x)}Pd_x$ films. We determined the exchange stiffness constant A, the uniaxial anisotropy constant $K_\perp$ and the saturation magnetization M for each of our four films from variable-temperature vibrating sample magnetometry (VSM), performed in the same way as described in detail in [11]. As might be expected, the Pd enrichment and concomitant loss of chemical order reduced the exchange stiffness constant A, anisotropy constant $K_\perp$ and saturation magnetization M_s, with all three quantities shown in relation to S in table 1.

We used magnetic force microscopy (MFM) to image the magnetic domain structure of our $L1_0$ $Fe_{(1-x)}Pd_x$ films at room temperature in zero field, as shown in figure 2(a)–(d). All four samples show the dense labyrinth domain patterns typical for these high perpendicular anisotropy films [18–20]. The samples were demagnetized using an alternating magnetic field of decreasing amplitude prior to imaging. The cantilevers had a resonant frequency of 65 kHz and a spring constant of 1–5 N m^{-1}. The CoCr-coated Si tip was vertically magnetized prior to imaging, and for optimal contrast we kept the tip–surface distance constant at a typical value ranging from 20 to 25 nm. The average magnetic domain width of the demagnetized state was deduced by a power-spectrum analysis, and the average domain widths of all four samples $\bar{D}_{\mathrm{MFM}}$ are listed in table 1. It can be seen that there is only a very weak dependence of the stripe domain period on S. The error bars were determined from the peak width of the dominant spatial frequencies in our power spectra.

We employed the magnetic parameters from our VSM measurements to carry out micromagnetic simulations of the domain structures in each sample using the OOMMF code [21]. The results are shown in figures 2(e)–(h), and are again listed with the degree of crystallographic long-range ordering in table 1. The cell size used was (1×1) nm^2 within the film plane and 15 nm perpendicular to the film plane. Although thermal activation effects are not taken into account in this type of micromagnetic code, we were nevertheless able to simulate the domain structures in our material at finite temperatures using appropriate values of the micromagnetic parameters $A(T)$, $K(T)$ and $M(T)$, since we are not concerned with activation over energy barriers but with equilibrium states. (A was scaled in proportion to the magnetization, as appropriate in mean field theory.) We have previously shown that the domain stripe period and wall thickness are rather insensitive to temperature [11, 14]. The average simulated domain width $\bar{D}_{\mathrm{sim}}$ in each of our four FePd samples as listed in table 1 is obtained from a Fourier analysis of the OOMMF output. Moreover, the average domain width evaluated from MFM images of all four samples $\bar{D}_{\mathrm{MFM}}$ agrees with $\bar{D}_{\mathrm{sim}}$ to within the error bar, see table 1, corroborating the correctness of the micromagnetic parameters determined from the VSM data. The domain widths and error bars were determined from a similar power spectrum analysis of the outputs from the simulations as that performed on the MFM images. While the changes in A and $K_\perp$ are substantial, the DW thickness $\delta_{\mathrm{W}} \sim \pi\sqrt{A/K_\perp} \approx 10$ nm has effectively no dependence on S (see table 1). Such narrow Bloch walls are characteristic for systems with high $K_\perp$, and our values relate closely to those obtained before by us [11, 14] and to those of other groups [22, 23]. Hence, the domain structures of all four films are very similar quantitatively as well as qualitatively.

3. Magnetotransport in the diffusive regime and diffusive current spin polarization

The diffusive electron transport properties of sheet films were measured at 4.5 K using a standard four-probe dc technique. Film resistivity ρ depends strongly on S, as might be expected, with data measured at 1.5 T—a single domain state—given in table 1. Hence, it is clear that the additional Pd atoms that disrupt the chemical ordering act as scattering centres and shorten the overall relaxation time of the electrons. However, it is remarkable that the total DW MR $\Delta\rho/\rho$ exhibits a strong enhancement with decreasing S in our FePd films, as shown in figure 3. The inset of figure 3 shows some example MR data, and the DWs give rise to the hysteretic part. The measured MR data were corrected for 12% of the total signal, attributable to anisotropic MR arising from the Néel caps of the Bloch DWs, based on micromagnetic

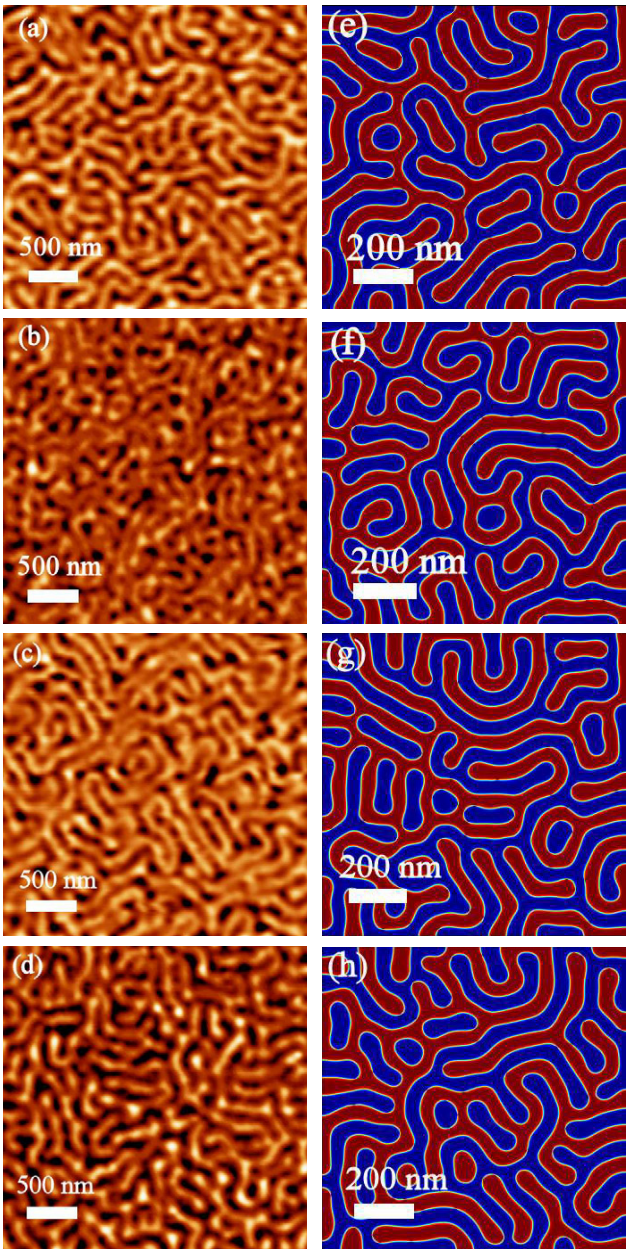

Figure 2. Magnetic force micrographs of our $L1_0$ $Fe_{(1-x)}Pd_x$ samples ((a) $S = 0.39$, (b) $S = 0.53$, (c) $S = 0.72$ and (d) $S = 0.80$) illustrating the labyrinth domain pattern typical for this magnetic material at the demagnetized state in zero applied field and at room temperature. For purposes of direct comparison, we performed micromagnetic simulations of this domain state ((e) $S = 0.39$, (f) $S = 0.53$, (g) $S = 0.72$ and (h) $S = 0.80$) employing sample-specific magnetic parameters such as saturation magnetization $M(T)$, exchange stiffness constant $A(T)$ and uniaxial anisotropy constant $K_{\perp}(T)$ determined from variable-temperature VSM. Note the differing scale bars in the experimental and simulated images.

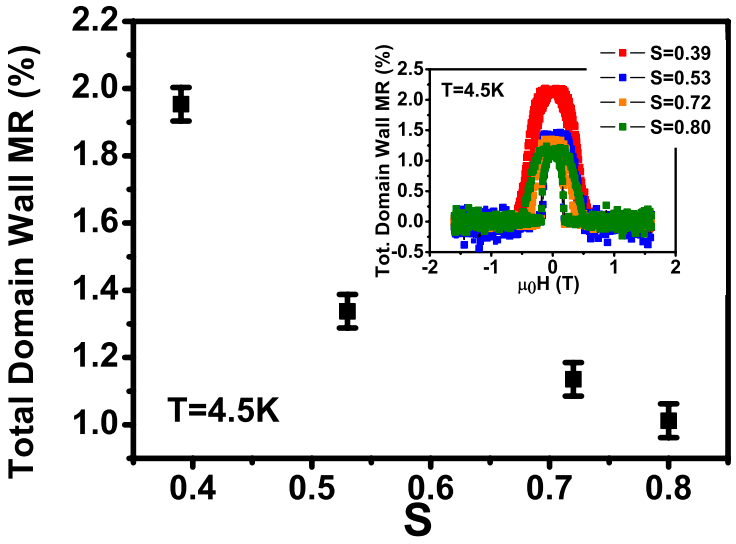

Figure 3. Total MR due to Bloch-type DWs for various chemical order parameters in $L1_0$-ordered epitaxial FePd films of approximately 30 nm thickness. The inset shows the typical hysteretic behaviour of the MR obtained by a four-probe dc measurement on a sheet film at $T = 4.5$ K.

modelling described below [14], before being plotted in the main panel. Hence, the additional resistance presented by a DW has increased by a greater proportion than the saturated ρ. It is worthwhile contrasting these data with those of Yu *et al*, who studied FePt films grown by molecular beam epitaxy [24]. In that experiment S was decreased by lowering the substrate temperature during growth while x was fixed, maintaining the values of M_s and A, while $K_\perp$ dropped precipitously. This led to a marked expansion in δ_W and a concomitant loss of DW MR, the opposite trend with S to that observed in our samples. This rise in DW MR in increasingly disordered samples is a key experimental result in this work, and requires an explanation. It is clear that the disorder has led to a rise in the overall scattering rate, since the resistivity of the films has risen. If this were to have taken place disproportionately in the minority Mott spin-channel, then the current would be more highly polarized, which would manifest itself in a higher DW MR.

Hence, in order to make our study quantitative, we have treated our DW MR data within the LZ spin-mixing model [5], one of the most widely used theories of DW MR that has successfully explained experimental features of the effect such as its dependence on DW thickness [25] and anisotropy with respect to current direction [22, 26]. In this model the resistivity due to DW scattering for both current perpendicular and current parallel to the Bloch-type DW is expressed explicitly as a function of the spin-asymmetry parameter $\alpha_{\text{diffusive}}$ [5, 11, 14, 22, 26, 27] and the spin mistracking parameter ξ, defined below. It uses the same Hamiltonian that governs giant MR [28], and employs a scattering potential

$$V_{\text{scattering}}(\mathbf{r}) = \sum_i [v(\mathbf{r}) + j(\mathbf{r})\sigma \cdot \hat{\mathbf{M}}(\mathbf{r})]\delta(\mathbf{r} - \mathbf{r}_i) \tag{5}$$

to describe the spin-dependent electron scattering, with impurity potential $v(\mathbf{r})$ at position $\mathbf{r}_i$, where $j(\mathbf{r})$ denotes the spin dependence of electron scattering, σ represents the Pauli matrices and $\hat{\mathbf{M}}(\mathbf{r})$ is the unit vector along the direction of local magnetization. Henceforth, for

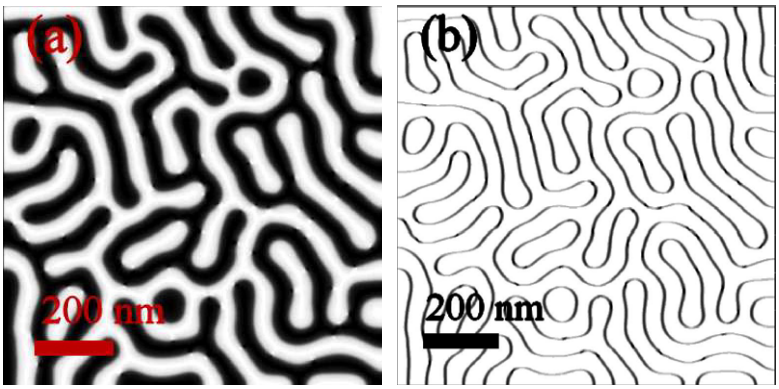

Figure 4. (a) Micromagnetic simulation of the stripe domain structure of a $1 \times 1\,\mu\text{m}^2$ slab of the $S = 0.39$ film. The dark and bright areas depict regions of opposite magnetization oriented perpendicular to the film plane and separated by Bloch DWs. (b) Local DW resistance for the simulated domain state depicted in (a), assuming a current flow from left to right in straight and direct paths. The DWs that are perpendicular to the current direction are seen to be darker, a result of the higher DW MR in CPW geometry.

simplicity in notation we write α for the diffusive spin asymmetry in conductance (defined by equation (3)).

While we measure the MR of the entire film, the LZ model describes the MR only where magnetization gradients exist, i.e. the DWs. Hence it is necessary to account for the domain pattern in our films, which was accomplished using our OOMMF simulations. An example of a simulated domain pattern is shown in figure 4(a), for $S = 0.39$. From this we calculate $\Theta = \arccos(M_z/M)$ and the local magnetization gradient $\nabla\Theta$, which determines the local strength of the spin mistracking $\xi = \hbar^2 k_\text{F} \nabla\Theta / 4mJ$, where $k_\text{F} \approx 2\,\text{Å}^{-1}$ is the Fermi wavevector, J is the Stoner exchange splitting and m is the effective mass, which we assume to be the free electron mass for the s-like majority spin carriers. This was done by setting J in our best ordered sample to the value of 1 eV based on the band structure calculation for a perfect crystal [29], and reducing it in proportion to the measured exchange stiffness A for each sample.

For this analysis, we decompose the current into components that are parallel (CIW) and perpendicular (CPW) to the magnetic domain wall as it meanders in order to calculate the local DW MR for our $1 \times 1\,\mu\text{m}^2$ slab:

$$\frac{\Delta\rho}{\rho} = \frac{(\xi)^2}{5}\cos^2(\beta)F_\text{CPW}(\alpha) + \frac{(\xi)^2}{5}\sin^2(\beta)F_\text{CIW}(\alpha), \tag{6}$$

where β is the local angle between $\nabla\Theta$ and the current direction. This type of angular dependence was recently confirmed experimentally by Aziz *et al* [26]. $F_\text{CIW}(\alpha)$ and $F_\text{CPW}(\alpha)$ describe the α-dependence of DW resistivity, and were taken as defined by Levy and Zhang [5, 14].

A computational result of the local DW MR determined based on equation (6) and the local magnetization of figure 4(a) is shown in figure 4(b), and we performed this procedure for all four samples (see figure 5(a)) based on the micromagnetic simulation results shown in figures 2(e)–(h). The darker contrast outlines the magnetic domain walls, representing significantly enhanced local resistivity due to the process of spin mixing in the region of rotating

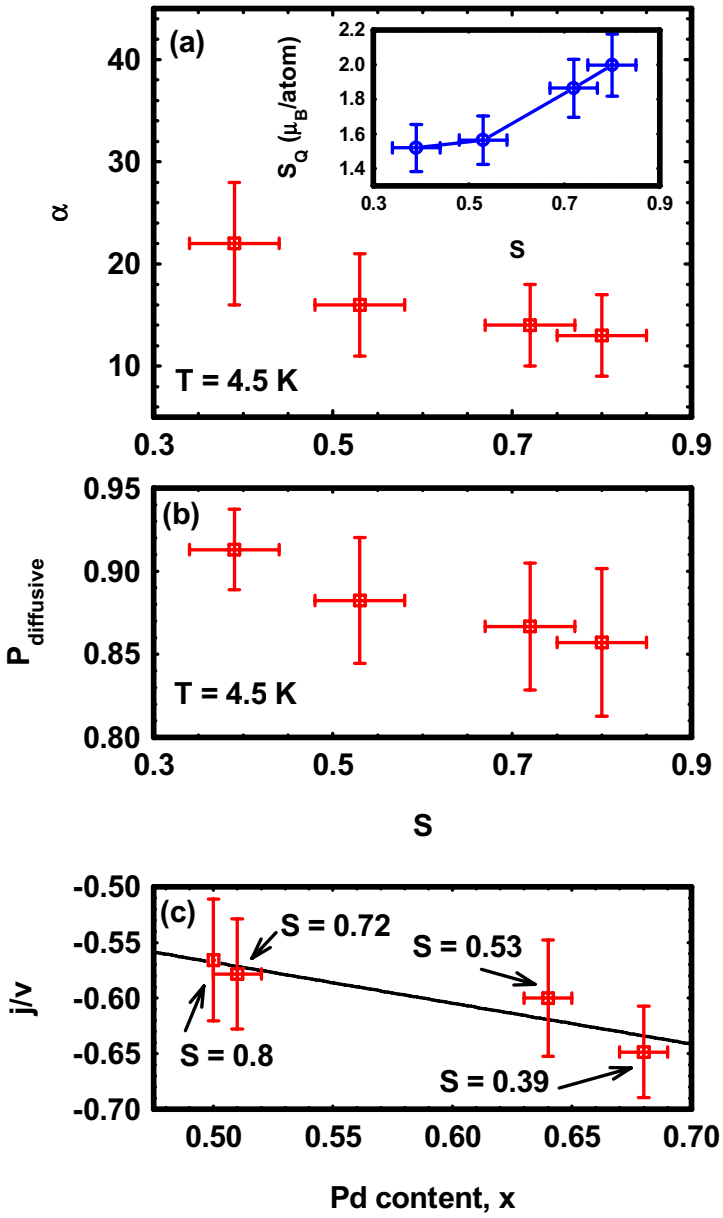

Figure 5. (a) The diffusive spin-asymmetry parameter α derived from DWR data and OOMMF simulations versus chemical long-range order parameter S. The inset shows the dependence of the average moment per atom S_{Q} on the order parameter S. We convert the diffusive spin-asymmetry parameter α directly into a current spin polarization valid for the diffusive electron transport regime (b), as outlined in equation (1) in the text. Despite high diffusive spin polarizations $P_{\mathrm{diffusive}}$, we obtain an increasing trend with lower chemical long-range ordering parameter S, reflecting the α dependency shown in (a). Evolution of the spin-dependent exchange scattering of a conduction electron normalized to its Coulomb scattering j/v on elemental Pd content in $\mathrm{L1_0}$ $\mathrm{Fe_{(1-x)}Pd_x}$. The ratio j/v was evaluated from α and equation (11). Error bars in all three plots show absolute uncertainties.

Table 2. Transport properties of the four $Fe_{1-x}Pd_x$ epilayers studied, labelled by their crystallographic long-range ordering S. The directly measured parameters are low-temperature (4.2 K) film resistivities ρ and the MR ratio due to magnetic domain walls (DW MR) at the same temperature. From these we inferred the spin conductance asymmetry parameter α and the diffusive current spin polarization $P_{\text{diffusive}}$ in direct comparison to the absolute value of the normalized conduction electron exchange scattering j/v for the four $L1_0$ $Fe_{1-x}Pd_x$ epilayers studied. The error bars given in these three quantities are derived from the measured values of the experimental data, such as the DW MR ratio, A, $K_\perp$, M_s, propagated through the formulae given in the text, either analytically or numerically. The ballistic current spin polarization $P_{\text{ballistic}}$, as evaluated by PCAR, is also tabulated for reasons of completeness and easy comparison. The error bars given here are absolute ones, including all possible sources of uncertainty in the measured input parameters.

S	ρ ($\mu\Omega$ cm)	DW MR (%)	α	$P_{\text{diffusive}}$	j/v	$P_{\text{ballistic}}$
0.39 ± 0.05	17 ± 3	2.0 ± 0.1	22 ± 6	0.91 ± 0.02	-0.65 ± 0.04	0.50 ± 0.05
0.53 ± 0.05	18 ± 4	1.3 ± 0.1	16 ± 5	0.88 ± 0.04	-0.60 ± 0.05	0.53 ± 0.05
0.72 ± 0.05	9 ± 3	1.1 ± 0.1	14 ± 4	0.87 ± 0.04	-0.58 ± 0.05	0.50 ± 0.05
0.80 ± 0.05	9 ± 2	1.0 ± 0.1	13 ± 4	0.86 ± 0.04	-0.57 ± 0.05	0.49 ± 0.11

localized spins of a magnetic domain wall, with the darkest contrast where the current crosses the walls in CPW geometry. Integrating over the entire region according to an equipotential summation algorithm (analogous to the mean of the Voigt and Reuss averages in Young's modulus of a composite [30]), with ρ fixed to the value for the film of interest, yielded the total simulated DW MR. The value of α was then varied in an iterative process until the simulated DW MR matched the measured value—the results are shown in figure 5(a) and table 2.

For the best ordered sample, we obtained a value of $\alpha \approx 12$ similar to those found previously in both MBE-grown FePd [14] and sputtered FePt [11]. The value of α rises to just over 20 as the Pd enrichment degrades the $L1_0$ ordering. This suggests that the additional Pd scattering centres that increase the resistivity have a strong spin-dependent cross-section. The inset of figure 5(a) shows S_Q, the average moment per atom derived from the low-temperature M_s data, versus S, indicating that additional Pd atoms do not exert their spin dependence of scattering via an enhanced localized moment. We note that in the literature obtained on similar systems, values for α for scattering from Pd impurities in Fe are not available, although the isoelectronic elements Ni and Pt show values of $\alpha \approx 7$–8 [31]. While elemental Fe is a weak ferromagnet, FePd has enough electrons to be a strong ferromagnet, consistent with higher values of α. Adding Pd adds electrons, pushing the Fermi level still higher above the top of the majority d-band. We proceeded to compute the current spin polarizations of the diffusive transport regime from equation (1), and the results are plotted in figure 5(b). All the samples have $P_{\text{diffusive}} \sim 85$–$90\%$, with the more highly polarized currents flowing in the less ordered samples.

To understand the effect of excess Pd scattering centres, we directly derive an expression for α in terms of the spin dependence of scattering j from the LZ model. Essentially, the

spin-channel resistivity ρ_σ is a function of the spin-dependent scattering time $[\tau_\sigma(\mathbf{k})]^{-1}$, considering that the spin-dependent Fermi $\mathbf{k}$-vectors do not differ in absolute value in a first-order approximation. (Here σ labels the spin state.) Hence, $\rho_\sigma \propto [\tau_\sigma(\mathbf{k})]^{-1}$ and we can resort to evaluating the ratio of the spin-dependent scattering rates in order to obtain the ratio α of the resistivities in both Mott channels. We express the conductivity of the magnetic domain wall in current-in-wall (CIW) geometry, i.e. the current flows parallel to the wall, without loss of generality as we are eventually interested only in ratios of conductivities:

$$\sigma = \frac{e}{8\pi^3}\sum_\sigma \int \frac{n_\sigma(\mathbf{k})}{|\mathbf{E}|}\frac{\hbar k_y}{m^*}\delta(E_F - \epsilon_{\mathbf{k}\sigma})\mathrm{d}^3\mathbf{k} \tag{7}$$

$$= \frac{e^2}{16\pi^3}\sum_\sigma \int \left(\frac{\hbar k_y}{m^*}\right)^2 \tau_\sigma(\mathbf{k})\delta(E_F - \epsilon_{\mathbf{k}})\mathrm{d}^3\mathbf{k}, \tag{8}$$

with $n_\sigma(\mathbf{k})$ denoting the spin density of states and m^* the effective electron mass.

Calculating the resistivity asymmetry amounts to finding the ratio of the scattering lifetimes, or rates ($W^{\sigma\sigma}_{\mathbf{k}\mathbf{k}'}$), which have the following dependence on the Coulomb (v) and exchange (j) potential parameters:

$$W^{\sigma\sigma}_{\mathbf{k}\mathbf{k}'} = \frac{2\pi}{\hbar}\frac{c_i}{N^2(k_x)N^2(k'_x)}\left[(v+\sigma j) + \frac{k_x k'_x}{k_F^2}\xi^2(v-\sigma j)\right]^2. \tag{9}$$

We then evaluate the spin-scattering rates ($W^{\sigma\sigma}_{\mathbf{k}\mathbf{k}'}$) in the limit of an infinite magnetic wall thickness. Here c_i refers to the concentration of impurity sites, and is an average counting over all such sites, where each site is taken to be of equivalent weighting. Taking the limit for infinite wall width, which amounts to taking the limit $\xi \to 0$, we find the ratio in the unperturbed spin-dependent resistivities, which is the quantity given by the Mott spin-channel resistivity asymmetry $\alpha = \rho_0^\uparrow/\rho_0^\downarrow$. This represents the scattering in the spin channel σ and directly leads us to a closed form of α in terms of the spin-dependent exchange scattering of conduction electrons based on the matrix elements of the scattering potentials $V^{\sigma\sigma}_{\mathbf{k}'\mathbf{k}}$ from which the spin-dependent scattering rates are calculated within the Mott channels. We now have the relation that can be calculated by considering the resistivity ratio of the spin-up and spin-down channels in the metal in the approximation, whereby the Fermi wavevectors in the spin sub-bands are identical:

$$\left(\frac{v-\sigma j}{v+\sigma j}\right)^2 = \frac{\rho_0^{-\sigma}k_{F-\sigma}^2}{\rho_0^{\sigma}k_{F\sigma}^2} = \alpha. \tag{10}$$

This yields α as a function of the spin-dependent exchange scattering of a conduction electron passing through a magnetic domain wall normalized to the strength of pure Coulomb scattering,

$$\alpha = \left(\frac{(j/v)-1}{(j/v)+1}\right)^2, \tag{11}$$

where v and j are as defined for equation (5). (A detailed derivation is given in [32], but the same result follows from the approximation that $1/\tau \propto V^2_{\mathrm{scatt}}$ [5].) From this we can see that the underlying cause of the high values of α and $P_{\mathrm{diffusive}}$ is a strong spin dependence of the scattering, as might intuitively be expected. Using equation (11) we can quantify the ratios j/v from our values of α for the four samples, which are shown in table 2—these can be taken as effective values averaged over all the scattering centres in each film. In figure 5(c) we show the dependence of the ratio j/v on x, which have a fairly linear relationship with each other.

This supports the picture of the additional Pd atoms, lying on Fe sites in the lattice, acting as additional scattering centres, which have a large spin-dependent cross-section, increasing the average j/v for all the scattering taking place in the material. This additional scattering in one spin channel leads to a high polarization in the diffusive current.

4. Point contact Andreev reflection (PCAR) spectroscopy and ballistic current spin polarization

A common method that is used to determine the spin polarization of a metallic material is to perform PCAR spectroscopy measurements [12, 13], where a superconducting tip is touched onto the surface of the ferromagnet to be studied. The central concept in this electron transport measurement is that for applied bias voltages within the energy gap of the superconductor, it is physically impossible to inject or extract single electrons, but only Cooper pairs, so that only the unpaired fraction of the current is transmitted in the sub-gap regime. This is compared to the full current for higher bias where quasiparticles may be injected. One then applies the modified Blonder–Tinkham–Klapwijk (BTK) theory [33, 34] to evaluate a bulk material value of the current spin polarization in the ballistic electron transport regime. In the version of the model we used, there are four numerical fitting parameters [34–36] to fit the measured conductance curves and thus determine the bulk current spin polarization of the sample. These are the broadening energy parameter ω, the barrier strength Z, which accounts for the cleanness of the interface and consequently quantifies the degree of interface scattering (e.g. an infinite Z accounts for a tunnel transport regime), the superconducting gap parameter Δ (we expect the bulk niobium value of $\sim$1.5 meV for our tips [36]) and, finally, the spin polarization $P_{\text{ballistic}}$ of the carriers crossing the interface.

We followed the common methodology of making, measuring and breaking a series of point contacts to each of our four samples, and then fitting each spectrum with the extended BTK model. We used a Nb tip and measurements were performed with the samples immersed in liquid He at 4.2 K. The details of our experimental and fitting procedures are identical to those described in [11, 36]. As an example of the type of data this yields, we show in the inset of figure 6 a typical conductance curve obtained in a PCAR measurement: in this case for the $S = 0.53$ sample, after correction for a spreading resistance, a parasitic ohmic resistance contribution arising from sheet film resistivity [37]. As previously [11, 36], the spreading resistance was estimated by rescaling the fitted gap from the raw data to the one that we have measured for the Nb tip. We collected multiple PCAR spectra of this sort for each of our samples with the resistance of the nanoscale contact between the superconducting niobium tip and the ferromagnetic film ranging from 3 to 9 Ω.

Again by way of example, the values of all four fitting parameters are plotted in figure 7 as a function of the point contact resistance (R) for the set of individual contacts achieved for the $S = 0.39$ sample. The broadening energy parameter ω is larger than $\omega \approx 0.36$ meV, the energy equivalent to the boiling point of helium $T = 4.2$ K, the real temperature of the experiment, as illustrated in figure 7(a) [34, 38]. This is because it includes all processes, both thermal and athermal, that contribute to a broadening of the conductance spectra. It can be seen from the data shown in figure 7(b), for one and the same niobium tip, that there is no clear dependence of the point contact resistance R and Z. This indicates that R is mainly determined by the size of the contact rather than by its interfacial scattering strength as long as the contact size is within the Sharvin limit [11, 34]. In addition to scattering centres caused by disorder or a surface oxide barrier, a $Z = 0$ contact is impossible, in principle, between dissimilar metals due

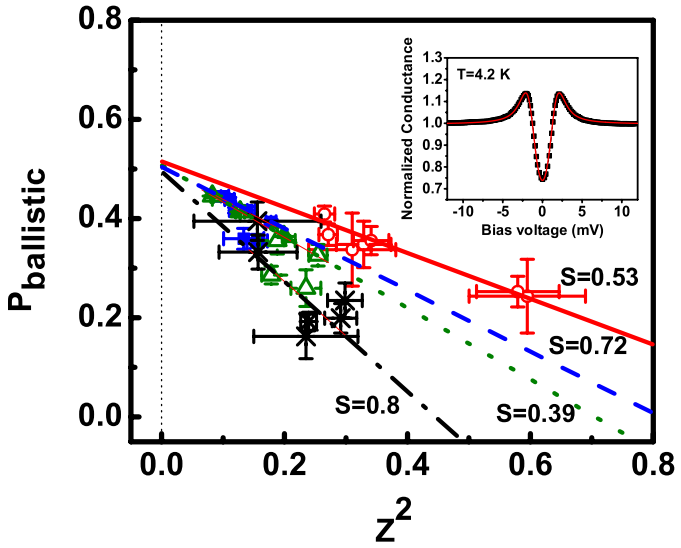

Figure 6. Ballistic current spin polarization versus the square of the superconductor-ferromagnet interface transparency parameter Z for $L1_0$-ordered FePd. Extrapolation of the least-squares fit (lines) onto the ordinate gives the bulk spin polarization of the current. The inset shows the normalized conductance versus the bias voltage spectrum as obtained by PCAR at $T = 4.2\,\mathrm{K}$ on the $S = 0.53$ sample, together with the respective fit to the modified BTK model, carried out using a Levenberg–Marquardt algorithm.

to Fermi velocity mismatch. Following the same procedure as in [36], the spreading resistance was estimated by rescaling the fitted gap from the raw data to the one that we have measured for the Nb tip. Finally, turning to the value of the ballistic current spin polarization itself as detailed in figure 7(d), it is obvious that spin polarization exhibits a nontrivial dependence on the contact resistance R between tip and sample.

As usual, however, there is a general declining trend in $P_{\mathrm{ballistic}}$ as Z rises, with the polarization dropping empirically as Z^2 [34, 39]. Figure 6 illustrates the ballistic current spin polarization $P_{\mathrm{ballistic}}$ as a function of the interface transparency parameter Z^2 for sequential contacts on all four FePd films. A scattering barrier at the metal/superconductor interface, which causes additional interfacial spin-scattering effects and thus diminishes the intrinsic polarization of the bulk material, has been put forward as the microscopic mechanism that accounts for such a decrease of $P_{\mathrm{ballistic}}$ with Z [34]. Conventional practice, which we follow, is to take the extrapolation of a least-squares fit to the case of a transparent interface ($Z^2 = 0$) to yield the value of the bulk spin polarization [3, 12, 13, 34], [39–41]. This procedure yields values of approximately $P_{\mathrm{ballistic}} \approx 0.5$ for all four samples, with no obviously apparent trend with S. The values we obtained for $P_{\mathrm{ballistic}}$ for each sample are shown in table 2 and are plotted in figure 8(b), with the error bars being the uncertainties in the ordinate intercepts of the straight line fits. These may be compared with the sample-to-sample variation in $P_{\mathrm{ballisitic}}$ of $\pm\sim 5\%$ that we estimated from a series of measurements of nominally identical Fe films.

5. Discussion

Comparing the current spin polarization results measured in the ballistic (plotted in figure 8(b)) and diffusive (replotted in figure 8(a) for easy comparison, but with systematic uncertainties in

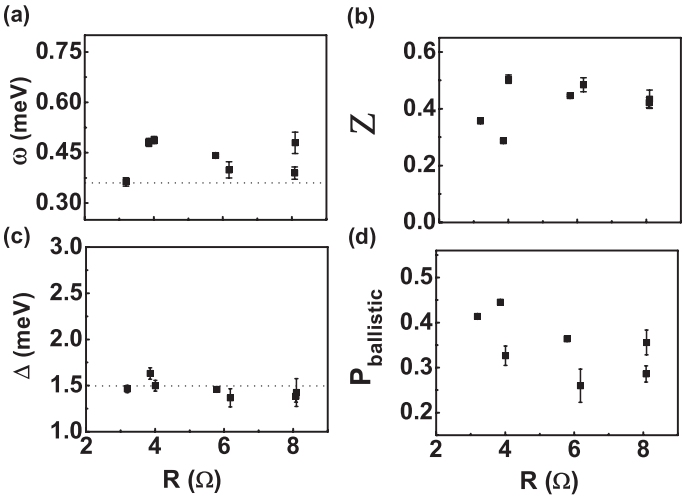

Figure 7. Dependence on contact resistance of the fitting parameters employed in the modified BTK model for the $S = 0.39$ FePd sample, i.e. the broadening energy parameter ω shown in (a), the barrier strength Z in (b), the superconducting gap parameter Δ in (c) and $P_{\text{ballistic}}$ plotted in (d). The dashed line in (a) points out $\omega \approx 0.36$ meV equivalent to the boiling point of liquid helium at $T = 4.2$ K. The dashed line in (c) marks the superconducting gap parameter $\Delta \approx 1.5$ meV of bulk niobium. In all four cases, the error bars are the standard errors returned by the fitting algorithm.

the error bar now neglected) regimes, there are two important conclusions that may be drawn. Firstly, we see that $P_{\text{diffusive}} > P_{\text{ballistic}}$ by roughly a factor of two in all cases, as we previously observed in the case of well-ordered FePt [11]. This observation extends the generality of that result to another isoelectronic material. Again, we interpret the difference as evidence that the scattering lifetimes $\tau_\uparrow$ and $\tau_\downarrow$ are significantly different, providing additional polarization of the current when diffusive currents flow.

Secondly, we may go further than this conclusion by noting that there is a dependence of $P_{\text{diffusive}}$ on the degree of chemical ordering, while $P_{\text{ballistic}}$ appears to be independent of S. Here we, in fact, use the parameter S as a convenient label for the samples, and would argue that the underlying cause of the rise in $P_{\text{diffusive}}$, manifested in higher DWMR, is the departure of x from the stoichiometric ideal of 0.5: the excess Pd atoms that reduce S act as extra scattering centres, raising ρ, with a strong spin dependence. These should only affect diffusive transport through the bulk of material, increasing $P_{\text{diffusive}}$, rather than ballistic transport through an interface, which should be unaffected. In PCAR spectroscopy experiments, as we probe for ballistic electron transport (or at least transport across the FePd/Nb interface where bulk scattering is irrelevant), there is no discernible dependence of the polarization on the sample, implying that $g(E_F)$ and v_F, and their spin dependence, are barely affected by the Pd enrichment, in spite of a marked reduction in magnetic moment per atom, which is reasonable since all these materials are strong ferromagnets with a similar contrast between the spin-↑ and spin-↓ carriers at the Fermi level. That there must be an upward trend in α and $P_{\text{diffusive}}$ with rising levels of disorder follows directly from the rise in the DW MR ratio displayed in figure 3.

It might be argued that the DW MR ratio could rise due to a decrease in the overall resistivity, which is to be found in the denominator of that ratio, an inspection of relevant data

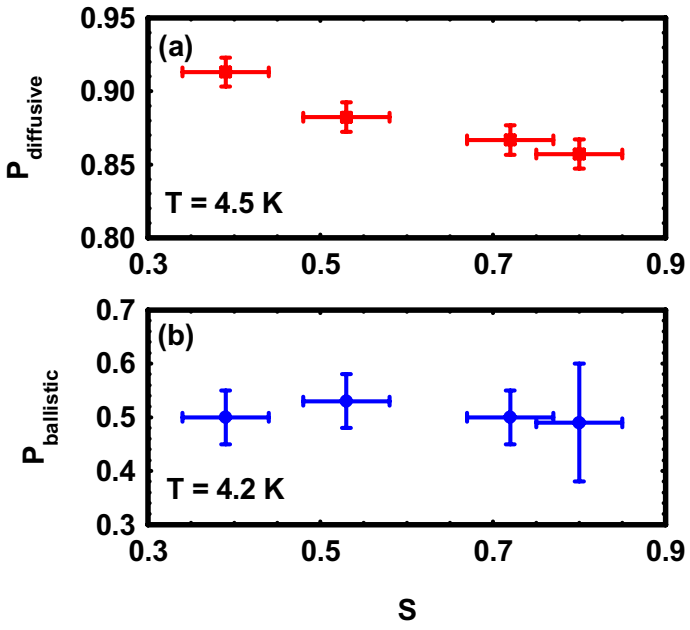

Figure 8. Comparison of the current spin polarization for various chemical order parameters of $L1_0$-phase FePd in both the diffusive (a) and the ballistic (b) transport regimes. Error bars in S are derived from the analysis of the x-ray diffraction data. Panel (a) reproduces the data from figure 5(b), but with only the random part of the uncertainty plotted as an error bar, in order to make the presence of a trend clear: the overall curve may hence be scaled by a constant that is uncertain by ± 0.015 in $P_{\text{diffusive}}$. The data in (b) are derived from our PCAR measurements, the error bars representing the uncertainty in the fitted intercept in the plot of $P_{\text{ballistic}}(Z^2)$.

for ρ in table 1 shows that this cannot be the case here. More subtly, it could be proposed that the decrease in the strength of the exchange interaction might be the underlying cause: through causing a narrower wall or a lower Larmor frequency in the exchange field, both of which will give rise to additional spin mistracking as the wall is traversed by an electron. Again from table 1, we can see that the anisotropy constant $K_\perp$ reduces in such a way as to hold the DW thickness δ_W almost unchanged, showing that the first of these two sets of circumstances is not relevant. The exchange strength does vary with S, but has also been quantitatively accounted for in the values of ξ that we have used to derive the type of data shown in figure 4: we are unable to reproduce our experimental MR data without allowing α to rise for the more disordered materials. Hence, we cannot avoid the conclusion that stronger spin-dependent scattering, leading to a more highly spin-polarized current, is the underlying mechanism for the rise in DW MR ratio that we have measured.

For both $P_{\text{diffusive}}$ and α, the total scattering rate is not relevant. Only the ratio of exchange scattering to Coulomb scattering j/v is important, which we have evaluated as shown in figure 5(b) and table 2. As we have several possible different types of scattering centres in our films (i.e. antisite Fe or Pd atoms, impurities or vacancies on either sublattice), we interpret these values as ensemble averages of j/v. This indicates that the spin dependence of scattering

at deliberately introduced excess Pd atoms is stronger than at spin-dependent scattering centres within the stoichiometric FePd matrix. This in turn gives rise to an enhanced average j/v, and the greater imbalance between $\tau_\uparrow$ and $\tau_\downarrow$ increases the spin polarization, and hence the DW MR as an experimental signature.

Going further and relating the spin-resistivity asymmetry parameter of the diffusive electron transport regime $\alpha_{\text{diffusive}}$ (see equation (3)) with the ballistic analogue defined in equation (2) gives $\alpha_{\text{diffusive}} = \alpha_{\text{ballistic}}(v_{\text{F}}^{\uparrow}\tau_\uparrow / v_{\text{F}}^{\downarrow}\tau_\downarrow)$. Hence, we find from the data shown in figure 8 a ratio of $[v_{\text{F}}^{\uparrow}\tau_\uparrow / v_{\text{F}}^{\downarrow}\tau_\downarrow]_{S=0.39} \approx 7$ for the lowest long-range order parameter to $[v_{\text{F}}^{\uparrow}\tau_\uparrow / v_{\text{F}}^{\downarrow}\tau_\downarrow]_{S=0.80} \approx 4$ in the case of the highest long-range order parameter within the FePd films investigated in this work. If we presume that the Fermi velocities change little with S on the basis of our PCAR data, then this change must be accounted for by an approximate halving of $\tau_\uparrow/\tau_\downarrow$. This is particularly important, as it suggests that control of the spin-dependent lifetimes may be possible through the selection of appropriate dopants as scattering centres, giving rise to the highly spin-polarized electron currents that are required for nanoscale spintronics: the spin polarization of a diffusive current is a key parameter in the theories that describe both spin-transfer torque experiments [42–44] and spin injection [45, 46].

6. Conclusion

To summarize our findings, we have studied a series of epitaxial thin-film samples of FePd alloys of increasing Pd enrichment. As might be expected, the additional Pd atoms degraded the degree of chemical ordering in the alloy and hence reduced the magnetocrystalline anisotropy. The reduction in the proportion of Fe atoms also reduced the magnetization. The resistivity of the films rose, consistent with additional Pd atoms acting as scattering centres for current-carrying electrons as the film chemical order is degraded.

However, the resistivity contribution arising from the ∼10 nm thick magnetic domain walls in the layers rose by a greater proportion than the magnetically saturated resistivity, indicating an increased degree of spin polarization of the current in this diffusive regime, where conductivity is limited by scattering. While our measurements cannot determine which spin carries the majority of the current, it is reasonable to assume from band-structure calculations that it is spin-↑. We also measured the spin polarization by a different technique, involving a superconducting PCAR, which is not affected by scattering within the magnetic material, and found no significant change. We conclude from these results that the additional Pd atoms act as highly spin-dependent scattering centres, which, while reducing the current that flows for a given applied electric field, increase the polarization of that current by selectively scattering out carriers of spin-↓ to a greater extent.

Acknowledgments

We thank S Zhang, G J Morgan, D M Edwards, A T Hindmarch, G Burnell, A Walton and M Ali for fruitful discussions. The authors also thank the UK National Grid Service along with J Berryman, J Lander and S Kaushal. This work was supported by the UK EPSRC (through the Spin@RT consortium) and the European Commission (through contract MRTN-CT-2003-504462, ULTRASMOOTH).

References

[1] Žutić I, Fabian J and Das Sarma S 2004 Spintronics: fundamentals and applications *Rev. Mod. Phys.* **76** 323

[2] Datta S and Das B 1990 Electronic analog of the electro-optic modulator *Appl. Phys. Lett.* **56** 665

[3] Marrows C H 2005 Spin-polarised currents and magnetic domain walls *Adv. Phys.* **54** 585

[4] Viret M, Vignoles D, Cole D, Coey J M D, Allen W, Daniel D S and Gregg J F 1996 Spin scattering in ferromagnetic thin films *Phys. Rev.* B **53** 8464

[5] Levy P M and Zhang S 1997 Resistivity due to domain wall scattering *Phys. Rev. Lett.* **79** 5110

[6] Berger L 1984 Exchange interaction between ferromagnetic domain wall and electric current in very thin metallic films *J. Appl. Phys.* **55** 1954

[7] Tatara G and Kohno H 2004 Theory of current-driven domain wall motion: spin transfer versus momentum transfer *Phys. Rev. Lett.* **92** 086601

[8] Stoner E C 1938 Collective electron ferromagnetism *Proc. R. Soc.* A **165** 372

[9] Mott N F and Jones H 1936 *The Theory of the Properties of Metals and Alloys* (Oxford: Oxford University Press)

[10] Mazin I I 1999 How to define and calculate the degree of spin polarization in ferromagnets *Phys. Rev. Lett.* **83** 1427

[11] Seemann K M, Baltz V, MacKenzie M, Chapman J N, Hickey B J and Marrows C H 2007 Diffusive and ballistic current spin polarization in magnetron-sputtered $L1_0$-ordered epitaxial FePt *Phys. Rev.* B **76** 174435

[12] Soulen R J *et al* 1998 Measuring the spin polarization of a metal with a superconducting point contact *Science* **282** 85

[13] Upadhyay S K, Palanisami A, Louie R N and Buhrman R A 1998 Probing ferromagnets with Andreev reflection *Phys. Rev. Lett.* **81** 3247

[14] Marrows C H and Dalton B C 2004 Spin mixing and spin-current asymmetry measured by domain wall magnetoresistance *Phys. Rev. Lett.* **92** 097206

[15] Warren B E 1969 *X-Ray Diffraction* (Reading, MA: Addison-Wesley)

[16] Macgillaury C H, Rieck G D and Lonsdale K (ed) 1962 *International Tables for X-Ray Crystallography* vol III (Birmingham: The Kynoch Press)

[17] Ibers J A and Hamilton W C (ed) 1974 *International Tables for X-Ray Crystallography* vol IV (Birmingham: The Kynoch Press)

[18] Thiele J-U, Folks L, Toney M F and Weller D K 1998 Perpendicular magnetic anisotropy and magnetic domain structure in sputtered epitaxial FePt (001) $L1_0$ films *J. Appl. Phys.* **84** 5686

[19] Barmak K, Kim J and Lewis L H 2005 On the relationship of magnetocrystalline anisotropy and stoichiometry in epitaxial $L1_0$ CoPt (001) and FePt (001) thin films *J. Appl. Phys.* **98** 033904

[20] Gehanno V, Marty A, Gilles B and Samson Y 1997 Magnetic domains in epitaxial ordered FePd(001) thin films with perpendicular magnetic anisotropy *Phys. Rev.* B **55** 12552

[21] Donahue M and Porter D G 1999 *OOMMF User's Guide, Version 1.0.* Interagency Report NISTIR 6376 (Gaithersburg, MD: National Institute of Standards and Technology)

[22] Viret M, Samson Y, Warin P, Marty A, Ott F, Søndergård E, Klein O and Fermon C 2000 Anisotropy of domain wall resistance *Phys. Rev. Lett.* **85** 3962

[23] Hinzke D, Kazantseva N, Nowak U, Mryasov O N, Asselin P and Chantrell R W 2008 Domain wall properties of FePt: from Bloch to linear walls *Phys. Rev.* B **77** 094407

[24] Yu J, Rüdiger U, Kent A D, Farrow R F C, Marks R F, Weller D, Folks L and Parkin S S P 2000 Magnetotransport and magnetic properties of molecular-beam epitaxy $L1_0$ FePt thin films *J. Appl. Phys.* **87** 6854

[25] Gordeev S N, Beaujour J-M L, Bowden G J, Rainford B D, de Groot P A, Ward R C, Wells M R and Jansen A G 2001 Giant magnetoresistance by exchange springs in $DyFe_2/YFe_2$ superlattices *Phys. Rev. Lett.* **87** 186808

[26] Aziz A, Bending S J, Roberts H G, Crampin S, Heard P J and Marrows C H 2006 Angular dependence of domain wall resistivity in artificial magnetic domain structures *Phys. Rev. Lett.* **97** 206602
[27] Ravelosona D, Cebollada A, Briones F, Diaz-Paniagua C, Hidalgo M A and Batallan F 1999 Domain-wall scattering in epitaxial FePd ordered alloy films with perpendicular magnetic anisotropy *Phys. Rev.* B **59** 4322
[28] Wang K, Zhang S and Levy P M 1996 Angular dependence of giant magnetoresistance in a superlattice *Phys. Rev.* B **54** 11965
[29] García D, Casero R, Vázquez M and Hernando A 2001 Calculated magnetocrystalline anisotropy of a FePd ordered alloy: electron-density dependence on the direction of magnetization *Phys. Rev.* B **63** 104421
[30] Ward I M and Sweeney J 2004 *An Introduction to the Mechanical Properties of Solid Polymers* (New York: Wiley)
[31] van den Berg H A M 2000 *Magnetic Multilayers and Giant Magnetoresistance: Fundamentals and Industrial Applications* (*Springer Series in Surface Sciences* vol 37) (Berlin: Springer) chapter 6, pp 179–262
[32] Hickey M C 2008 Calculated magneto-resistance due to domain walls: the role of impurity scattering arXiv:0805.0443
[33] Blonder G E, Tinkham M and Klapwijk T M 1982 Transition from metallic to tunneling regimes in superconducting microconstrictions: excess current, charge imbalance and supercurrent conversion *Phys. Rev.* B **25** 4515
[34] Strijkers G J, Ji Y, Yang F Y, Chien C L and Byers J M 2001 Andreev reflections at metal/superconductor point contacts: measurement and analysis *Phys. Rev.* B **63** 104510
[35] Bugoslavsky Y, Miyoshi Y, Clowes S K, Branford W R, Lake M, Brown I, Caplin A D and Cohen L F 2005 Possibilities and limitations of point-contact spectroscopy for measurements of spin polarization *Phys. Rev.* B **71** 104523
[36] Baltz V, Naylor A D, Seemann K M, Elder W, Sheen S, Westerholt K, Zabel H, Burnell G, Marrows C H and Hickey B J 2009 Conductance features in point contact Andreev reflection spectra *J. Phys.: Condens. Matter* **21** 095701
[37] Woods G T, Soulen R J Jr, Mazin I I, Nadgorny B, Osofsky M S, Sanders J, Srikanth H, Egelhoff W F and Datla R 2004 Analysis of point-contact Andreev reflection spectra in spin polarization measurements *Phys. Rev.* B **70** 054416
[38] Kant C H, Kurnosikov O, Filip A T, LeClair P, Swagten H J M and de Jonge W J M 2002 Origin of spin-polarization decay in point-contact Andreev reflection *Phys. Rev.* B **66** 212403
[39] Ji Y, Strijkers G J, Yang F Y, Chien C L, Byers J M, Anguelouch A, Xiao G and Gupta A 2001 Determination of the spin polarization of half-metallic CrO_2 by point contact Andreev reflection *Phys. Rev. Lett.* **86** 5585
[40] de Jong M J M and Beenakker C W J 1995 Andreev reflection in ferromagnet-superconductor junctions *Phys. Rev. Lett.* **74** 1657
[41] Nadgorny B, Mazin I I, Osofsky M, Soulen R J, Broussard P, Stroud R M, Singh D J, Harris V G, Arsenov A and Mukovskii Y 2001 Origin of high transport spin polarization in $La_{0.7}Sr_{0.3}MnO_3$: direct evidence for minority spin states *Phys. Rev.* B **63** 184433
[42] Berger L 1978 Low-field magnetoresistance and domain drag in ferromagnets *J. Appl. Phys.* **49** 2156
[43] Zhang S and Li Z 2004 Roles of nonequilibrium conduction electrons on the magnetization dynamics of ferromagnets *Phys. Rev. Lett.* **93** 127204
[44] Thiaville A, Nakatani Y, Miltat J and Suzuki Y 2005 Micromagnetic understanding of current-driven domain wall motion in patterned nanowires *Europys. Lett.* **69** 990
[45] Schmidt G, Ferrand D, Molenkamp L W, Filip A T and van Wees B J 2000 Fundamental obstacle for electrical spin injection from a ferromagnetic metal into a diffusive semiconductor *Phys. Rev.* B **62** 4790
[46] Fert A and Jaffrès H 2001 Conditions for efficient spin injection from a ferromagnetic metal into a semiconductor *Phys. Rev.* B **64** 184420